

ND-SDF: LEARNING NORMAL DEFLECTION FIELDS FOR HIGH-FIDELITY INDOOR RECONSTRUCTION

Ziyu Tang¹, Weicai Ye^{1,2,✉}, Yifan Wang², Di Huang², Hujun Bao¹, Tong He^{2,✉}, Guofeng Zhang¹

¹State Key Lab of CAD&CG, Zhejiang University, ²Shanghai AI Laboratory

<https://zju3dv.github.io/nd-sdf/>

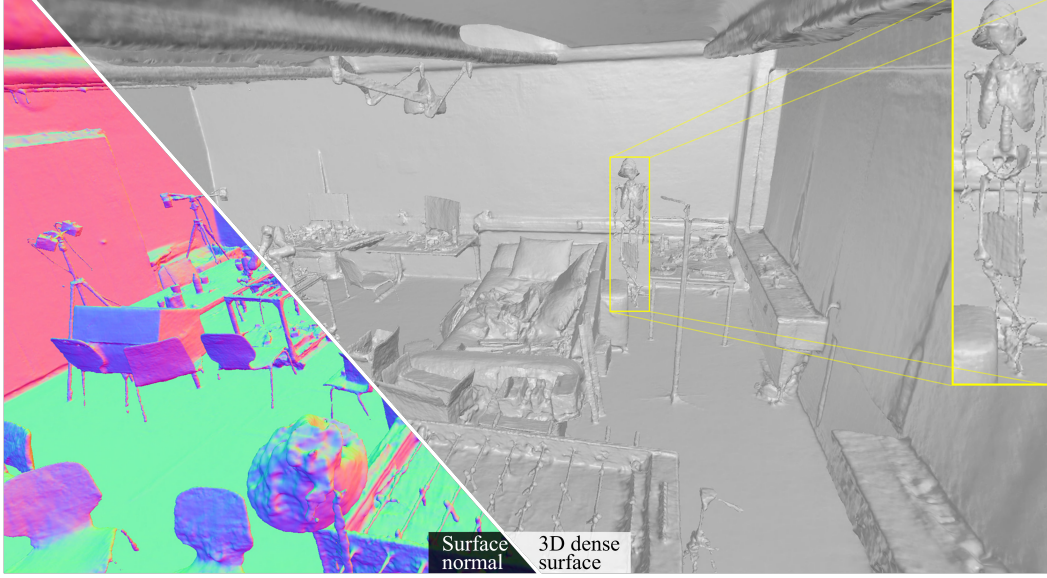


Figure 1: We present **ND-SDF**, a framework for high-fidelity 3D indoor surface reconstruction from multi-views. Shown above is an extracted mesh from ScanNet++.

ABSTRACT

Neural implicit reconstruction via volume rendering has demonstrated its effectiveness in recovering dense 3D surfaces. However, it is non-trivial to simultaneously recover meticulous geometry and preserve smoothness across regions with differing characteristics. To address this issue, previous methods typically employ geometric priors, which are often constrained by the performance of the prior models. In this paper, we propose **ND-SDF**, which learns a **N**ormal **D**eflection field to represent the angular deviation between the scene normal and the prior normal. Unlike previous methods that uniformly apply geometric priors on all samples, introducing significant bias in accuracy, our proposed normal deflection field dynamically learns and adapts the utilization of samples based on their specific characteristics, thereby improving both the accuracy and effectiveness of the model. Our method not only obtains smooth weakly textured regions such as walls and floors but also preserves the geometric details of complex structures. In addition, we introduce a novel ray sampling strategy based on the deflection angle to facilitate the unbiased rendering process, which significantly improves the quality and accuracy of intricate surfaces, especially on thin structures. Consistent improvements on various challenging datasets demonstrate the superiority of our method.

1 INTRODUCTION

3D surface reconstruction Chen et al. (2024); Ye et al. (2024b;a); Wang et al. (2024); Ye et al. (2022; 2023b); Liu et al. (2021); Li et al. (2020) aims to recover watertight, dense 3D geometry from multi-view images Hartley & Zisserman (2003), representing a significant research area in computer vision and graphics. The recovered surfaces have proven invaluable for many downstream tasks, including robotic navigation, AR/VR, and smart cities.

Recently, coordinate-based networks Mildenhall et al. (2021); Barron et al. (2022); Müller et al. (2022); Martin-Brualla et al. (2021); Zhang et al. (2020); Ye et al. (2023a); Huang et al. (2024); Ming et al. (2022) are drawing increasing attention, due to their remarkable performance in the task of novel view synthesis. Inspired by the implicit representation of the scene, many subsequent works introduced SDF Park et al. (2019) or occupancy Li et al. (2022) to parameterize the 3D geometry.

However, recovering high-fidelity surfaces remains challenging, as relying solely on color images for supervision often results in an underconstrained problem, especially for regions like textureless walls and ceilings. Previous methods Yu et al. (2022b); Wang et al. (2022) have attempted to mitigate this issue by incorporating auxiliary supervision. For instance, MonoSDF employs monocular cues from a pretrained model as pseudo-ground truth to supervise the model, which partially alleviates the problem in textureless areas. However, the large errors due to domain gaps in monocular cues and the inconsistencies in view-dependent prior guidance often lead to visible detail loss and erroneous surfaces, as depicted in Figure 3 of the experimental section.

Noting that prior models are highly accurate in simpler regions like floors and walls but struggle with complex geometries, we introduce ND-SDF for high-fidelity indoor reconstruction (Figure 1). Our core innovation is the construction of a deflection field that adaptively learns the geometric deviations between the actual scene geometry and the prior geometry derived from normal priors. The inherent deviation is defined as the angular difference between the true scene normals and the prior normals. By aligning the deflected scene normals with the normal cues, our model can adaptively learn the deviation, which encourages accurate recovery of intricate structures maintaining fine details without being misled by erroneous priors.

In addition, we propose a novel adaptive deflection angle prior loss that leverages prior normals for differential supervision of high and low-frequency areas, achieving an optimal balance between smoothness and detail. Our observations indicate that large angle deviations are primarily concentrated in thin and fine-grained structures. Building on this insight, we introduce deflection-angle guided optimization to proactively facilitate the recovery of detailed structures. Furthermore, we address a significant bias issue and propose deflection angle-guided unbiased rendering to improve the reconstruction of small or thin structures, as shown in Figure 1. In summary, we present the following contributions:

- We propose a novel scene attribute field, named normal deflection field, which adaptively learns the deviations between the scene and normal priors. This method aids us in distinguishing between detailed and textureless areas. Therefore, we can restore more fine structures while ensuring the smoothness and integrity of the scene.
- Empirically assuming that prior models incur larger errors in complex areas, we employ the deflection angle to discriminate between high and low-frequency regions. Consequently, we propose a novel adaptive deflection angle prior loss that dynamically adjusts the utilization of distinct cues, thereby achieving a balance between complex structures and smooth surfaces. Furthermore, we utilize the deflection angle to guide ray sampling and photometric optimization, facilitating the restoration of finer-grained structures.
- To address the inherent bias issue of neural surface rendering, we integrate the unbiasing method Zhang et al. (2023) to implement an adaptive, unbiased rendering strategy. This approach facilitates the recovery of extremely thin structures without compromising scene fidelity. Our method outperforms previous approaches significantly in indoor reconstruction evaluations, and this superiority is validated through extensive ablation experiments.

2 RELATED WORK

Neural Surface Representation of 3D scenes Recently, the representation of 3D scenes using neural fields has gained popularity due to their expressiveness and simplicity. NeRF-type approaches Mildenhall et al. (2021); Barron et al. (2022); Müller et al. (2022); Fridovich-Keil et al. (2022); Sun et al. (2022) have proposed encoding coordinate-based density and appearance of scenes by utilizing simple multilayer perceptrons (MLPs) and explicit structures such as voxel grids, resulting in photorealistic novel view synthesis. However, these approaches fail to accurately recover surfaces due to the lack of constraints on density. To address this issue, subsequent works, such as VolSDF Yariv et al. (2021) and Neus Wang et al. (2021), implicitly represent signed distance functions (SDFs) and employ a SDF-density conversion function to encourage precise surface reconstruction. Other methods Li et al. (2023); Rosu & Behnke (2023); Wang et al. (2023); Yariv et al. (2023); Fu et al. (2022); Zhang et al. (2023) have also been proposed, introducing different representations and optimization techniques to further enhance reconstruction quality and efficiency. Nevertheless, these aforementioned methods struggle to handle indoor scenes with a large number of low-frequency areas (e.g., walls and floors), as photometric loss becomes unreliable in such regions.

Neural reconstruction in Indoor Environments Due to the complex layouts of indoor scenes, additional auxiliary data are required for reasonable reconstruction. Manhattan-SDF Guo et al. (2022) employs the Manhattan assumption and semantic priors to jointly regularize textureless regions such as walls and floors. HelixSurf Liang et al. (2023) achieves intertwined regularization iteratively by combining neural implicit surface learning with PatchMatch-based multi-view stereo (MVS) Barnes et al. (2009) robustly and efficiently. Other works Yu et al. (2022b); Wang et al. (2022) propose utilizing monocular priors from pretrained models to achieve smooth and complete reconstruction. However, directly applying normal or depth priors Yu et al. (2022b) may lead to undesirable reconstruction results due to the unreliable nature of these priors. NeuRis Wang et al. (2022) filters out unreliable priors based on the assumption that areas with rich 2D visual features are more error-prone. H2O-SDF Park et al. (2024) simply utilizes prior uncertainty to re-weight the normal prior loss. Nevertheless, both of these methods exhibit weak generalization capabilities. For example, the visual feature hypothesis Wang et al. (2022) struggles to differentiate between rich-textured planar areas. Similarly, prior-guided re-weighting Park et al. (2024) is further constrained by the domain gap between the prior model and the scene. On the other hand, DebSDF Xiao et al. (2024) effectively designs an uncertainty field based on a probabilistic model to guide the loss function, leading to more robust and accurate reconstructions. In contrast to methods with weaker generalization capabilities and those relying on probabilistic models, our proposed method, ND-SDF, learns a Normal Deflection field that enables the dynamic adaptation of priors based on their characteristics. This field directly models geometrically meaningful $SO(3)$ residuals, resulting in highly detailed surface reconstructions while maintaining smoothness and robustness.

3 METHOD

The primary objective of our Normal Deviation Signed Distance Function (ND-SDF) is to reconstruct dense surfaces from calibrated multi-view images, with a primary focus on indoor scenes with established priors. To achieve this, we introduce a novel component known as the normal deflection field. This field is designed to quantify and learn the deviations between actual scene geometries and their corresponding normal priors. By integrating this field, our method can adaptively supervise both high and low-frequency regions in the scene. This adaptive supervision is crucial for preserving fine details while ensuring overall surface smoothness.

The operational framework of our approach is depicted in Figure 2. In subsequent sections, we delve into a comprehensive discussion on the implementation of the normal deflection field. Additionally, we explore various strategies that leverage this field to enhance the fidelity of surface details, thereby promoting a more accurate surface reconstruction.

3.1 PRELIMINARIES

Volume Rendering NeRF assumes that a ray $\mathbf{r}(t) = \mathbf{o} + t\mathbf{v}$ is emitted from viewpoint \mathbf{o} in direction \mathbf{v} , where t denotes the distance from the viewpoint. N points are sampled on the ray, i.e. $\mathbf{x}_i =$

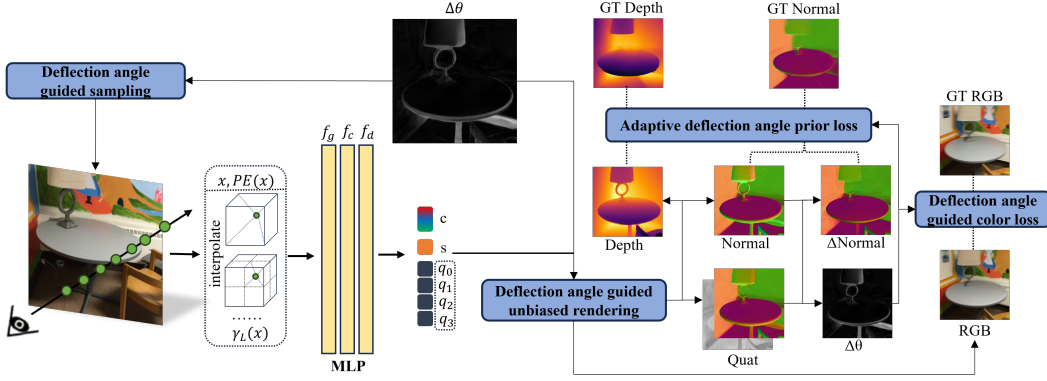


Figure 2: **Overview of our method.** We utilize multi-resolution hash grids γ_L as scene representation. The core of ND-SDF is the normal deflection field. We represent deflection with quaternions, which are predicted by the deflection network (denoted as f_d). We align the deflected normals with the prior normals to learn the deviation between the scene and the priors. To distinctly supervise high and low-frequency areas, we employ an adaptive deflection angle prior loss, ensuring both smoothness and detail. Furthermore, we utilize the deflection angle $\Delta\theta$ to distinguish complex structures, enabling angle-guided sampling and color loss to facilitate intricate surface details. Lastly, we combine the unbiased rendering method Zhang et al. (2023) to ensure the generation of extremely thin structures indoors.

$\mathbf{o} + t_i \mathbf{v}, i \in \{1, 2, \dots, N\}$. Given each point's volume density σ_i and color \mathbf{c}_i , the color of the ray can be synthesized using volume rendering techniques as:

$$\hat{\mathbf{C}}(\mathbf{r}) = \sum_{i=1}^N T_i \alpha_i \mathbf{c}_i, \quad \alpha_i = 1 - \exp(-\sigma_i \delta_i), \quad T_i = \prod_{j=1}^{i-1} (1 - \alpha_j), \quad (1)$$

where α is the opacity of i -th ray segment, T denotes the transmittance rate, $\delta_i = t_i - t_{i-1}$ denotes distance between adjacent samples.

A color loss supervising the rendered color and ground-truth color is utilized to optimize the network:

$$\mathcal{L}_{\text{color}} = \sum_{\mathbf{r} \in \mathcal{R}} \|\hat{\mathbf{C}}(\mathbf{r}) - \mathbf{C}(\mathbf{r})\|_1, \quad (2)$$

where \mathcal{R} is the sampled ray set.

SDF-induced Volume Rendering The rise of neural surface reconstruction is attributed to methods like VolSDF and Neus, which propose specific SDF to volume density representation, allowing optimization with volume rendering. The final surface, denoted as S , is equivalent to the zero level-set of the implicit distance field, i.e., $S = \{\mathbf{x} \in \mathbb{R}^3 | s(\mathbf{x}) = 0\}$, where $s(\mathbf{x})$ is the SDF value.

We follow VolSDF, employing the Laplace Cumulative Distribution Function(CDF) to model the relationship between SDF and volumetric density:

$$\sigma(\mathbf{x}) = \frac{1}{\beta} \Psi_{\beta}(-s(\mathbf{x})) = \begin{cases} \frac{1}{2\beta} \exp\left(\frac{-s(\mathbf{x})}{\beta}\right) & \text{if } s(\mathbf{x}) \leq 0 \\ \frac{1}{\beta} - \frac{1}{2\beta} \exp\left(\frac{s(\mathbf{x})}{\beta}\right) & \text{if } s(\mathbf{x}) > 0 \end{cases}, \quad (3)$$

where Ψ_{β} denotes the Laplace CDF, β denotes the variance. The depth $\hat{D}(\mathbf{r})$ and normal $\hat{\mathbf{N}}(\mathbf{r})$ of the surface intersection point is synthesized using volume rendering technology:

$$\hat{D}(\mathbf{r}) = \sum_{i=1}^N T_i \alpha_i t_i, \quad \hat{\mathbf{N}}(\mathbf{r}) = \sum_{i=1}^N T_i \alpha_i \mathbf{n}_i, \quad (4)$$

where \mathbf{n}_i is the analytical gradient of the SDF network. Following MonoSDF Yu et al. (2022b), we utilize monocular depth and normal generated by pretrained model Eftekhar et al. (2021) to supervise the rendered depth and normal:

$$\mathcal{L}_{\text{depth}} = \sum_{\mathbf{r} \in \mathcal{R}} \|w \hat{D}(\mathbf{r}) + q - D(\mathbf{r})\|^2, \quad \mathcal{L}_{\text{normal}} = \sum_{\mathbf{r} \in \mathcal{R}} \|\hat{\mathbf{N}}(\mathbf{r}) - \mathbf{N}(\mathbf{r})\|_1 + \left\| 1 - \hat{\mathbf{N}}(\mathbf{r})^T \mathbf{N}(\mathbf{r}) \right\|_1, \quad (5)$$

where the two coefficients (w, q) obtained by least square algorithms are utilized to align the scale between monocular depth and rendered depth, i.e., $w\hat{D} + q \approx D$.

We encode scene geometry using Instant-NGP Müller et al. (2022) γ_L and a shallow MLP f_g , that is, $(s(\mathbf{x}) \in \mathbb{R}^3, \mathbf{z}(\mathbf{x}) \in \mathbb{R}^{256}) = f_g(\mathbf{x}, PE(\mathbf{x}), \gamma_L(\mathbf{x}))$, where $\mathbf{z}(\mathbf{x})$ denotes the latent geometry feature.

Also, we utilize the eikonal term Gropp et al. (2020); Yariv et al. (2020) to regularize the shape of SDF in 3D space:

$$\mathcal{L}_{\text{eik}} = \frac{1}{N} \sum_{i=1}^N (\|\nabla s(\mathbf{x}_i)\|_2 - 1)^2, \quad (6)$$

Following Neuralangelo Li et al. (2023), we further employ numerical gradients to enhance surface geometric consistency and use curvature loss for smoothness. The detailed definitions of them are provided in the appendix.

3.2 NORMAL DEFLECTION FIELD

A significant challenge in indoor 3D reconstruction is achieving a balance between the smoothness of surfaces and the intricacy of complex structures. Traditional approaches relying solely on photometric loss have proven inadequate for accurately capturing smooth areas, particularly in texture-deficient regions. These methods often necessitate auxiliary data, such as normal priors, to enhance the reconstruction quality in textureless areas. However, the uniform application of normal priors across different scene types can impair the recovery of complex structures. This is primarily due to the variable reliability of these priors in diverse regions, where they may not accurately reflect the underlying geometry. To address this issue, we propose the development of a Normal Deflection field. This field is designed to dynamically represent the deviation between the actual scene normals and the provided normal priors. By doing so, it effectively circumvents the potential misguidance from inconsistent priors, thereby enabling a more reliable and nuanced reconstruction of both smooth and complex indoor structures.

We choose quaternion as the deflection form, which is a lightweight rotation representation. The quaternion can be parameterized by a single MLP f_d :

$$\mathbf{q}_i = f_d(\mathbf{x}_i, \mathbf{v}_i, \mathbf{n}_i, \mathbf{z}_i), \quad (7)$$

where $\mathbf{q}_i = (\mathbf{q}_i^0, \mathbf{q}_i^1, \mathbf{q}_i^2, \mathbf{q}_i^3)$ is the deflection quaternion(normalized default) of sampled \mathbf{x}_i . Quaternion at the surface intersection point is synthesized using volume rendering technology, similar to how NeRF synthesizes colors:

$$\mathbf{Q}(\mathbf{r}) = \sum_{i=1}^N T_i \alpha_i \mathbf{q}_i, \quad (8)$$

We deflect the rendered normal using the composed deflection quaternion $\mathbf{Q}(\mathbf{r})$:

$$\hat{\mathbf{N}}^d(\mathbf{r}) = \mathbf{Q}(\mathbf{r}) \otimes \hat{\mathbf{N}}(\mathbf{r}) \otimes \mathbf{Q}^{-1}(\mathbf{r}), \quad (9)$$

where $\hat{\mathbf{N}}^d$ denotes the deflected rendered normal, \mathbf{Q}^{-1} denotes the inverse of \mathbf{Q} , also known as the conjugate, and \otimes is a quaternion multiplication operation. Since a quaternion can be represented in trigonometric form, i.e. $\mathbf{Q} = \cos \frac{\theta}{2} + \sin \frac{\theta}{2}(\mathbf{u}^1 i, \mathbf{u}^2 j, \mathbf{u}^3 k)$, this operation is to rotate the rendered normal around the quaternion axis $\mathbf{u} = (\mathbf{u}^1, \mathbf{u}^2, \mathbf{u}^3)$ by θ degrees.

The deviation between the scene and priors is learned by minimizing the difference between the deflected rendered normal and the prior normal. Thus, we define the deflected normal loss:

$$\mathcal{L}_{\text{normal}}^d = \sum_{\mathbf{r} \in \mathcal{R}} \|\hat{\mathbf{N}}^d(\mathbf{r}) - \mathbf{N}(\mathbf{r})\|_1 + \left\| 1 - \hat{\mathbf{N}}^d(\mathbf{r})^T \mathbf{N}(\mathbf{r}) \right\|_1, \quad (10)$$

3.3 ADAPTIVE DEFLECTION ANGLE PRIOR LOSS

The learned deviation is defined as the deflection angle($\Delta\theta$) of the rendered normal:

$$\Delta\theta = \arccos(\hat{\mathbf{N}}(\mathbf{r}) \cdot \hat{\mathbf{N}}^d(\mathbf{r})), \quad (11)$$

where $\Delta\theta \in [0, \pi]$, Empirically, the deviation between the scene and priors increases as the structure becomes more complex. It leads to an intuitive conclusion that the deflection angle is small in smooth areas and large in high-frequency areas. The adaptive deflection angle normal prior loss is proposed to dynamically adjust the utilization of differing priors based on their characteristics:

$$\mathcal{L}_{normal}^{ad} = \frac{\sum_{\mathbf{r} \in \mathcal{R}} g^d(\Delta\theta) \mathcal{L}_{normal}^d(\hat{\mathbf{N}}^d(\mathbf{r}), \mathbf{N}(\mathbf{r}))}{g(\Delta\theta) \mathcal{L}_{normal}(\mathbf{N}(\mathbf{r}), \mathbf{N}(\mathbf{r}))}, \quad (12)$$

where g^d and g are modulation functions that adjust the weight of the deflected and original normal loss term based on the deflection angle. We similarly define an adaptive depth prior loss:

$$\mathcal{L}_{depth}^{ad} = \sum_{\mathbf{r} \in \mathcal{R}} g(\Delta\theta) \mathcal{L}_{depth}(\hat{D}(\mathbf{r}), D(\mathbf{r})). \quad (13)$$

As $\Delta\theta$ increases, $g^d(\Delta\theta)$ increases, and $g(\theta)$ decreases, since we should less apply priors in complex areas indicated by large deflection angles. The combined adaptive normal and depth prior loss is referred to as the adaptive deflection angle prior loss (see appendix for detailed definitions).

3.4 DEFLECTION ANGLE GUIDED OPTIMIZATION

Through the utilization of the proposed adaptive prior loss, we dynamically adjust the utilization of various priors, significantly enhancing the quality of reconstruction. However, this alone is insufficient for generating more complex structures. Fundamentally, merely learning the deviation does not endow the capability to reconstruct additional details. Recognizing that large deflection angles indicate complex areas, we introduce three deflection angle guided optimization methods designed to facilitate the recovery of thinner and more fine-grained structures.

Deflection angle guided sampling. Textureless areas, such as walls, constitute a significant portion of indoor scenes. These areas converge rapidly by utilizing priors. To prevent continuous oversampling of well-learned smooth regions, we proactively sample more rays in complex areas to capture finer details. The sampling process is guided by the deflection angles (see supplementary for details).

Deflection angle guided photometric loss. To further promote the recovery of details, we impose additional photometric loss on complex areas indicated by the deflection angles. We re-weight the original color loss guided by the deflection angle, resulting in the re-weighted color loss:

$$\mathcal{L}_{color}^d = \sum_{\mathbf{r} \in \mathcal{R}} w_{color}(\Delta\theta(\mathbf{r})) \|\hat{\mathbf{C}}(\mathbf{r}) - \mathbf{C}(\mathbf{r})\|_1, \quad (14)$$

where $\Delta\theta(\mathbf{r})$ denotes the deflection angle of sampled ray \mathbf{r} , and w_{color} is the re-weight function guided by $\Delta\theta$.

Deflection angle guided unbiased rendering. Accurately reconstructing thin structures, such as chair legs, remains challenging. This limitation arises from inherent bias issues in SDF-induced volume rendering, manifesting in two ways: (1) According to TUVZ Zhang et al. (2023), the derivative of the rendering weight $\frac{\partial w(t)}{\partial t}$ is influenced by various angle differences between ray directions and scene normals. This results in a non-maximum value of w at the surface intersection point, reducing surface quality. (2) For rays passing close to the object, the Laplace CDF assigns high density to points near the surface of the ray, leading to incorrect rendering depths and normals. This issue causes thin structures to gradually disappear during training. Therefore, it is crucial to apply an unbiased rendering method during reconstruction.

Following TUVZ Zhang et al. (2023), we transform SDF to density using an unbiased function:

$$\sigma(\mathbf{r}(t_i)) = \alpha \Psi_\beta \left(\frac{-f_g(\mathbf{r}(t_i))}{|f'_g(\mathbf{r}(t_i))|} \right), \quad (15)$$

where $\mathbf{r}(t_i) = \mathbf{o} + t_i \mathbf{v}$ represents a sampled point on the ray, and f_g is the geometry network, which predicts the SDF value. This transformation effectively alleviates bias issues. However, we observe that simply applying it results in the surface failing to converge. Hence, we only partially apply it to thin structures indicated by the learned deflection angles.

Method	Acc↓	Comp↓	Pre↑	Recall↑	Chamfer↓	F-score↑
COLMAP Schönberger et al. (2016)	0.047	0.235	71.1	44.1	0.141	53.7
Unisurf Oechsle et al. (2021)	0.554	0.164	21.2	36.2	0.359	26.7
VolSDF Yariv et al. (2021)	0.414	0.120	32.1	39.4	0.267	34.6
Neus Wang et al. (2021)	0.179	0.208	31.3	27.5	0.194	29.1
NeuRIS Wang et al. (2022)	0.050	0.049	71.7	66.9	0.050	69.2
MonoSDF Yu et al. (2022b)	0.035	0.048	79.9	68.1	0.042	73.3
HelixSurf Liang et al. (2023)	0.038	0.044	78.6	72.7	0.042	75.5
Ours	0.032	0.044	84.9	73.5	0.038	78.6

Table 1: **Quantitative results on the ScanNet dataset.** We achieve state-of-the-art performance.

Method	Auditorium	Ballroom	Courtroom	Museum	Mean
NeuRIS Wang et al. (2022)	0.79	0.84	2.78	1.34	1.13
MonoSDF Yu et al. (2022b)	3.17	3.70	13.75	5.68	6.58
Ours	4.37	6.45	16.28	10.30	9.35

Table 2: **F-score on the TanksandTemples dataset.**

3.5 OPTIMIZATION

The overall loss function is defined as:

$$\mathcal{L} = \mathcal{L}_{color}^d + \lambda_1 \mathcal{L}_{eik} + \lambda_2 \mathcal{L}_{curv} + \lambda_3 \mathcal{L}_{normal}^{ad} + \lambda_4 \mathcal{L}_{depth}^{ad}, \quad (16)$$

The weights $\lambda_1 \dots \lambda_4$ are utilized to balance the importance of these loss terms.

4 EXPERIMENT

Datasets We conducted experiments on four indoor datasets: ScanNet Dai et al. (2017), Replica Straub et al. (2019), TanksandTemples Knapitsch et al. (2017), and ScanNet++ Yeshwanth et al. (2023). ScanNet contains 1513 indoor scenes captured with an iPad, processed using the BundleFusion algorithm to obtain camera poses and surface reconstruction. Replica is a synthetic dataset comprising 18 indoor scenes. Each scene features dense geometry and high dynamic range textures. TanksandTemples is a large-scale 3D reconstruction dataset including high-resolution outdoor and indoor environments. We followed the splits from MonoSDF and applied the same evaluation settings. We also conduct experiments on ScanNet++, which includes 460 indoor scenes captured using laser scanners. These scenes offer high-quality dense reconstructions and images. For testing, we selected six scenes from ScanNet++.

Implementation details Our method was implemented using PyTorch Paszke et al. (2019). The image resolution for all scenes is 384×384. We obtained normal and depth cues using Omnidata. Multi-resolution hash grids were utilized for scene representation. Both the geometry network and color network consisted of two layers, each with 256 nodes. Our network was optimized using AdamW Loshchilov & Hutter (2017) optimizer with a learning rate of 1e-3. The weights for loss terms were: $\lambda_1 = 0.05$, $\lambda_2 = 0.0005$, $\lambda_3 = 0.025$, $\lambda_4 = 0.05$. Upon adequate initialization of the deflection field, we initiated deflection angle guided sampling, photometric optimization, and unbiased rendering. All experiments were conducted on an NVIDIA TESLA A100 PCIe 40GB, with each iteration sampling 4×1024 rays, totaling 128,000 training steps. The total training time was about 12 hours. Our hash encoding resolution spanned from 2^5 to 2^{11} across 16 levels, with the initial activation level set to 8 and activation steps to 2000.

Metrics In line with prior research, we employ six standard metrics to evaluate the reconstructed meshes: Accuracy, Completeness, Chamfer Distance, Precision, Recall, and F-score. Additionally, normal consistency is utilized for evaluating the Replica dataset.

Baselines We compare with the following methods: (1) Classic MVS COLMAP Schonberger & Frahm (2016); Schönberger et al. (2016); (2) Neural implicit methods including VolSDF and Neus; (3) Methods utilizing auxiliary data including MonoSDF and NeuRIS; (4) Other indoor reconstruction methods like HelixSurf Liang et al. (2023).

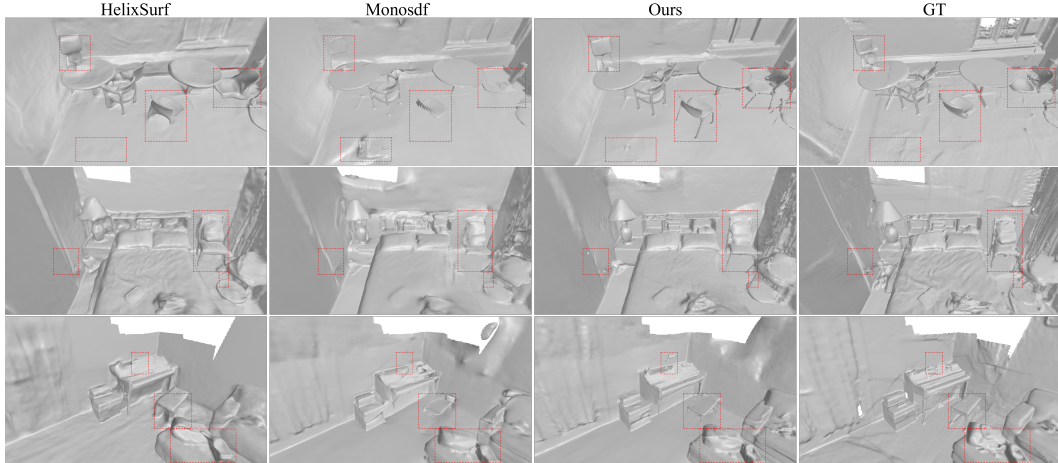


Figure 3: **Qualitative results on ScanNet.** Compared with previous state-of-the-art works, our method produces more thin and fine-grained structures, such as the chair legs and detailed table layouts.

4.1 COMPARISONS

ScanNet: In Figure 3, we present qualitative results and in Table 1, quantitative results are displayed. These quantitative results are averaged over the selected four scenes. ND-SDF surpasses previous best-performing works, achieving state-of-the-art performance. Specifically, we achieve the highest F-score, which serves as a credible indicator reflecting reconstruction accuracy by considering both Accuracy and Completeness. When compared with HelixSurf and MonoSDF (as shown in Figure 3), our approach accurately captures thin structures such as chair legs and lamp rings. This underscores the superiority of our proposed deflection methods, which significantly enhance the recovery of thin and fine-grained structures indoors.

Method	Acc↓	Comp↓	Pre↑	Recall↑	Chamfer↓	F-score↑
VolSDF Yariv et al. (2021)	0.070	0.102	0.405	0.339	0.086	0.368
Baked-Angelo Yu et al. (2022a)	0.152	0.039	0.543	0.718	0.095	0.614
MonoSDF Yu et al. (2022b)	0.057	0.032	0.651	0.703	0.044	0.675
Ours	0.056	0.024	0.667	0.785	0.040	0.721

Table 3: **Quantitative results on the ScanNet++ dataset.** We select 6 scenes and calculate the average metrics of them.

Method	Normal C.↑	Chamfer↓	F-score↑
Unisurf Oechsle et al. (2021)	90.96	4.93	78.99
MonoSDF Yu et al. (2022b)	92.11	2.94	86.18
Ours	92.85	2.57	91.6

Table 4: **Quantitative results of Replica dataset.**

Replica: Following MonoSDF Yu et al. (2022b), we used their pre-processed masks to filter out abnormal priors. We reported quantitative results in Table 4. Our approach achieves the highest F-score and the lowest Chamfer distance, substantially surpassing previous works. See supplementary for qualitative results.

Tanks and temples: We also conducted experiments on the advanced split of T&T, which provides several challenging large-scale indoor scenes. Quantitative results are provided in Table 2, where ND-SDF outperforms previous methods that utilize priors. Additional qualitative results can be found in the supplementary material, our method recovered substantial detailed structures.

ScanNet++: ScanNet++ comprises numerous complex indoor scenes, each offering high-resolution GT mesh and RGB data. Since no public results are available for ScanNet++, we trained some baselines using our settings, including VolSDF Yariv et al. (2021), MonoSDF Yu et al. (2022b), and Baked-Angelo Yu et al. (2022a). Among these, only MonoSDF utilized monocular priors. Our

Method	Omnidata Eftekhari et al. (2021)	Wizard Fu et al. (2024)
Base	0.700	0.661
Ours	0.750	0.730

Table 5: **F-score of Different Priors Models..**

Method	Base	ND	AP	DO	DU	—	Acc↓	Comp↓	Prec↑	Recall↑	Chamfer↓	F-score↑
Base	✓	×	×	×	×	—	0.046	0.046	0.576	0.640	0.046	0.606
ModelA	✓	✓	×	×	×	—	0.044	0.042	0.601	0.666	0.043	0.632
ModelB	✓	✓	✓	×	×	—	0.038	0.032	0.637	0.726	0.035	0.679
ModelC	✓	✓	✓	✓	×	—	0.040	0.030	0.631	0.740	0.035	0.681
Ours	✓	✓	✓	✓	✓	—	0.038	0.031	0.648	0.728	0.034	0.686

Table 6: **Quantitative Results of Ablation for Different Modules.** ‘Base’ can be considered as MonoSDF+Neuralangelo. ‘ND’ denotes applying the deflection field and the deflected normal loss term L_{normal}^d . ‘AP’ denotes the two adaptive deflection angle prior loss terms including L_{normal}^{ad} and L_{depth}^{ad} . ‘DO’ denotes the two deflection angle guided optimizations, namely sampling and photometric loss. ‘DU’ denotes the deflection angle guided unbiased rendering.

quantitative results are summarized in Table 3, demonstrating state-of-the-art performance across all metrics. For additional visualization results, please refer to the supplementary material.

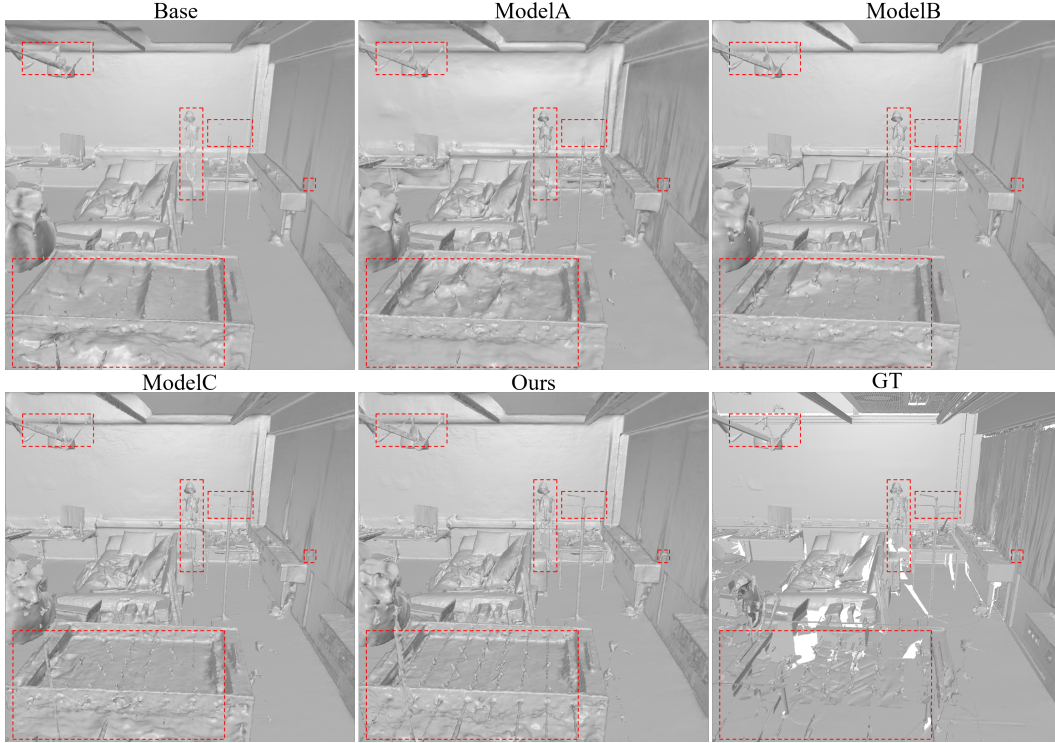


Figure 4: **Visualization Results of the Models after Ablation.**

4.2 ABLATION STUDY

4.2.1 ABLATION OF DIFFERENT MODULES

The learned deviations play a crucial role in locating high-frequency regions. Consequently, we employ deflection angles for sampling, photometric optimization, and unbiased rendering to facilitate the recovery of thin and fine-grained structures. We conducted detailed ablation experiments to assess the effectiveness of these modules, resulting in five post-ablation models: Base, ModelA, ModelB, ModelC, and Ours. For quantitative results and comprehensive definitions, please refer to Table 6. Figure 4 visually illustrates how the proposed components enhance overall performance.

Analysis of Normal Deflection Field The Base model strictly adheres to monocular cues, leading to significant detail loss due to misguided priors in complex areas. In ModelA, we introduced the deflection field and applied the deflected normal loss to learn deviations. The improvement in the F-score to 0.632 (as shown in Table 6) confirms the superiority of the deviation learning approach. However, we observed wrinkles (as depicted in Figure 4) in textureless regions like walls. This issue arises from the lack of constraints on deflection, resulting in inefficient utilization of priors in smooth areas. In ModelB, introducing an adaptive deflection angle prior loss significantly enhanced reconstruction quality, balancing both smoothness and detail.

Analysis of deflection angle guided optimization While ModelB substantially improves reconstruction quality compared to the Base, it still struggles with finer structures. In ModelC, we introduced deflection angle guided sampling and color loss to emphasize surface details. Finally, we incorporated deflection angle guided unbiased rendering to facilitate the recovery of thin structures. Figure 4 demonstrates that Ours recovers a wide range of complex and fine structures, including skull models, wires, and iron swabs, surpassing the Base model. As indicated in Table 6, Ours achieved the highest f-score, proving the effectiveness of the proposed modules for restoring high-fidelity surfaces.

4.2.2 ABLATION OF DIFFERENT PRIOR MODELS

Our method learns deviations between the scene and normal priors predicted by a specific pretrained model. It is essential to explore its effectiveness across different cues. To achieve this, we employed the currently state-of-the-art method Geowizard Fu et al. (2024) to generate both depth and normal cues. The quantitative results, as summarized in Table 5, demonstrate that our method significantly enhances surface quality regardless of the cues used. This experiment demonstrates the superiority of our method. It invariably improves reconstruction accuracy in scenarios where prior knowledge is used.

5 CONCLUSION

We have presented ND-SDF, a novel approach that learns deviations between the scene and normal priors for high-fidelity indoor surface reconstruction. We propose an adaptive deflection angle prior loss to dynamically supervise areas with varying characteristics. By identifying high-frequency regions based on deflection angles, we employ angle guided optimization to generate thin and fine-grained structures. Our method recovers a substantial amount of complex structures, as demonstrated by extensive qualitative and quantitative results that confirm its superiority. ND-SDF efficiently adapts to unreliable priors in challenging areas, significantly addressing the issue of detail loss caused by large prior errors for regions with fine structures.

Limitation ND-SDF is confined to reconstruction scenarios involving priors. Our approach exhibits limited capability in handling areas with less coverage. Due to inherent ambiguities in observations, the deflection field may learn incorrect structures and settle into local optima. We kindly refer the reader to the supplementary material for more analysis and results. In the future, we may explore multi-view consistency constraints to enhance reconstruction quality.

REFERENCES

- Connelly Barnes, Eli Shechtman, Adam Finkelstein, and Dan B Goldman. Patchmatch: A randomized correspondence algorithm for structural image editing. *ACM Trans. Graph.*, 28(3):24, 2009.
- Jonathan T Barron, Ben Mildenhall, Dor Verbin, Pratul P Srinivasan, and Peter Hedman. Mip-nerf 360: Unbounded anti-aliased neural radiance fields. In *Proceedings of the IEEE/CVF Conference on Computer Vision and Pattern Recognition*, pp. 5470–5479, 2022.
- Danpeng Chen, Hai Li, Weicai Ye, Yifan Wang, Weijian Xie, Shangjin Zhai, Nan Wang, Haomin Liu, Hujun Bao, and Guofeng Zhang. Pgsr: Planar-based gaussian splatting for efficient and high-fidelity surface reconstruction. *arXiv preprint arXiv:2406.06521*, 2024.
- Angela Dai, Angel X Chang, Manolis Savva, Maciej Halber, Thomas Funkhouser, and Matthias Nießner. Scannet: Richly-annotated 3d reconstructions of indoor scenes. In *Proceedings of the IEEE conference on computer vision and pattern recognition*, pp. 5828–5839, 2017.
- Ainaz Eftekhari, Alexander Sax, Jitendra Malik, and Amir Zamir. Omnidata: A scalable pipeline for making multi-task mid-level vision datasets from 3d scans. In *Proceedings of the IEEE/CVF International Conference on Computer Vision*, pp. 10786–10796, 2021.
- Sara Fridovich-Keil, Alex Yu, Matthew Tancik, Qinhong Chen, Benjamin Recht, and Angjoo Kanazawa. Plenoxels: Radiance fields without neural networks. In *Proceedings of the IEEE/CVF Conference on Computer Vision and Pattern Recognition*, pp. 5501–5510, 2022.
- Qiancheng Fu, Qingshan Xu, Yew Soon Ong, and Wenbing Tao. Geo-neus: Geometry-consistent neural implicit surfaces learning for multi-view reconstruction. *Advances in Neural Information Processing Systems*, 35:3403–3416, 2022.
- Xiao Fu, Wei Yin, Mu Hu, Kaixuan Wang, Yuexin Ma, Ping Tan, Shaojie Shen, Dahua Lin, and Xiaoxiao Long. Geowizard: Unleashing the diffusion priors for 3d geometry estimation from a single image. *arXiv preprint arXiv:2403.12013*, 2024.
- Amos Gropp, Lior Yariv, Niv Haim, Matan Atzmon, and Yaron Lipman. Implicit geometric regularization for learning shapes. *arXiv preprint arXiv:2002.10099*, 2020.
- Haoyu Guo, Sida Peng, Haotong Lin, Qianqian Wang, Guofeng Zhang, Hujun Bao, and Xiaowei Zhou. Neural 3d scene reconstruction with the manhattan-world assumption. In *Proceedings of the IEEE/CVF Conference on Computer Vision and Pattern Recognition*, pp. 5511–5520, 2022.
- Richard Hartley and Andrew Zisserman. *Multiple view geometry in computer vision*. Cambridge university press, 2003.
- Chenxi Huang, Yuenan Hou, Weicai Ye, Di Huang, Xiaoshui Huang, Binbin Lin, Deng Cai, and Wanli Ouyang. Nerf-det++: Incorporating semantic cues and perspective-aware depth supervision for indoor multi-view 3d detection. *arXiv preprint arXiv:2402.14464*, 2024.
- Arno Knapitsch, Jaesik Park, Qian-Yi Zhou, and Vladlen Koltun. Tanks and temples: Benchmarking large-scale scene reconstruction. *ACM Transactions on Graphics (ToG)*, 36(4):1–13, 2017.
- Hai Li, Weicai Ye, Guofeng Zhang, Sanyuan Zhang, and Hujun Bao. Saliency guided subdivision for single-view mesh reconstruction. In *2020 International Conference on 3D Vision (3DV)*, pp. 1098–1107. IEEE, 2020.
- Hai Li, Xingrui Yang, Hongjia Zhai, Yuqian Liu, Hujun Bao, and Guofeng Zhang. Vox-surf: Voxel-based implicit surface representation. *IEEE Transactions on Visualization and Computer Graphics*, 2022.
- Zhaoshuo Li, Thomas Müller, Alex Evans, Russell H Taylor, Mathias Unberath, Ming-Yu Liu, and Chen-Hsuan Lin. Neuralangelo: High-fidelity neural surface reconstruction. In *Proceedings of the IEEE/CVF Conference on Computer Vision and Pattern Recognition*, pp. 8456–8465, 2023.

-
- Zhihao Liang, Zhangjin Huang, Changxing Ding, and Kui Jia. Helixsurf: A robust and efficient neural implicit surface learning of indoor scenes with iterative intertwined regularization. In *Proceedings of the IEEE/CVF Conference on Computer Vision and Pattern Recognition*, pp. 13165–13174, 2023.
- Xiangyu Liu, Weicai Ye, Chaoran Tian, Zhaopeng Cui, Hujun Bao, and Guofeng Zhang. Cox-graph: multi-robot collaborative, globally consistent, online dense reconstruction system. In *2021 IEEE/RSJ International Conference on Intelligent Robots and Systems (IROS)*, pp. 8722–8728. IEEE, 2021.
- Ilya Loshchilov and Frank Hutter. Decoupled weight decay regularization. *arXiv preprint arXiv:1711.05101*, 2017.
- Ricardo Martin-Brualla, Noha Radwan, Mehdi SM Sajjadi, Jonathan T Barron, Alexey Dosovitskiy, and Daniel Duckworth. Nerf in the wild: Neural radiance fields for unconstrained photo collections. In *Proceedings of the IEEE/CVF Conference on Computer Vision and Pattern Recognition*, pp. 7210–7219, 2021.
- Ben Mildenhall, Pratul P Srinivasan, Matthew Tancik, Jonathan T Barron, Ravi Ramamoorthi, and Ren Ng. Nerf: Representing scenes as neural radiance fields for view synthesis. *Communications of the ACM*, 65(1):99–106, 2021.
- Yuhang Ming, Weicai Ye, and Andrew Calway. idf-slam: End-to-end rgb-d slam with neural implicit mapping and deep feature tracking. *arXiv preprint arXiv:2209.07919*, 2022.
- Thomas Müller, Alex Evans, Christoph Schied, and Alexander Keller. Instant neural graphics primitives with a multiresolution hash encoding. *ACM transactions on graphics (TOG)*, 41(4):1–15, 2022.
- Michael Oechsle, Songyou Peng, and Andreas Geiger. Unisurf: Unifying neural implicit surfaces and radiance fields for multi-view reconstruction. In *Proceedings of the IEEE/CVF International Conference on Computer Vision*, pp. 5589–5599, 2021.
- Jeong Joon Park, Peter Florence, Julian Straub, Richard Newcombe, and Steven Lovegrove. DeepSDF: Learning continuous signed distance functions for shape representation. In *Proceedings of the IEEE/CVF conference on computer vision and pattern recognition*, pp. 165–174, 2019.
- Minyoung Park, Mirae Do, YeonJae Shin, Jaeseok Yoo, Jongkwang Hong, Joongrock Kim, and Chul Lee. H2o-sdf: Two-phase learning for 3d indoor reconstruction using object surface fields. *arXiv preprint arXiv:2402.08138*, 2024.
- Adam Paszke, Sam Gross, Francisco Massa, Adam Lerer, James Bradbury, Gregory Chanan, Trevor Killeen, Zeming Lin, Natalia Gimelshein, Luca Antiga, et al. Pytorch: An imperative style, high-performance deep learning library. *Advances in neural information processing systems*, 32, 2019.
- Radu Alexandru Rosu and Sven Behnke. Permutosdf: Fast multi-view reconstruction with implicit surfaces using permutohedral lattices. In *Proceedings of the IEEE/CVF Conference on Computer Vision and Pattern Recognition*, pp. 8466–8475, 2023.
- Johannes L Schonberger and Jan-Michael Frahm. Structure-from-motion revisited. In *Proceedings of the IEEE conference on computer vision and pattern recognition*, pp. 4104–4113, 2016.
- Johannes L Schönberger, Enliang Zheng, Jan-Michael Frahm, and Marc Pollefeys. Pixelwise view selection for unstructured multi-view stereo. In *Computer Vision–ECCV 2016: 14th European Conference, Amsterdam, The Netherlands, October 11–14, 2016, Proceedings, Part III 14*, pp. 501–518. Springer, 2016.
- Julian Straub, Thomas Whelan, Lingni Ma, Yufan Chen, Erik Wijmans, Simon Green, Jakob J Engel, Raul Mur-Artal, Carl Ren, Shobhit Verma, et al. The replica dataset: A digital replica of indoor spaces. *arXiv preprint arXiv:1906.05797*, 2019.
- Cheng Sun, Min Sun, and Hwann-Tzong Chen. Direct voxel grid optimization: Super-fast convergence for radiance fields reconstruction. In *Proceedings of the IEEE/CVF Conference on Computer Vision and Pattern Recognition*, pp. 5459–5469, 2022.

-
- Jiepeng Wang, Peng Wang, Xiaoxiao Long, Christian Theobalt, Taku Komura, Lingjie Liu, and Wenping Wang. Neuris: Neural reconstruction of indoor scenes using normal priors. In *European Conference on Computer Vision*, pp. 139–155. Springer, 2022.
- Peng Wang, Lingjie Liu, Yuan Liu, Christian Theobalt, Taku Komura, and Wenping Wang. Neus: Learning neural implicit surfaces by volume rendering for multi-view reconstruction. *arXiv preprint arXiv:2106.10689*, 2021.
- Yifan Wang, Di Huang, Weicai Ye, Guofeng Zhang, Wanli Ouyang, and Tong He. Neurodin: A two-stage framework for high-fidelity neural surface reconstruction. *arXiv preprint arXiv:2408.10178*, 2024.
- Yiming Wang, Qin Han, Marc Habermann, Kostas Daniilidis, Christian Theobalt, and Lingjie Liu. Neus2: Fast learning of neural implicit surfaces for multi-view reconstruction. In *Proceedings of the IEEE/CVF International Conference on Computer Vision*, pp. 3295–3306, 2023.
- Yuting Xiao, Jingwei Xu, Zehao Yu, and Shenghua Gao. Debsdf: Delving into the details and bias of neural indoor scene reconstruction. *IEEE Transactions on Pattern Analysis and Machine Intelligence (TPAMI)*, 2024.
- Lior Yariv, Yoni Kasten, Dror Moran, Meirav Galun, Matan Atzmon, Basri Ronen, and Yaron Lipman. Multiview neural surface reconstruction by disentangling geometry and appearance. *Advances in Neural Information Processing Systems*, 33:2492–2502, 2020.
- Lior Yariv, Jiatao Gu, Yoni Kasten, and Yaron Lipman. Volume rendering of neural implicit surfaces. *Advances in Neural Information Processing Systems*, 34:4805–4815, 2021.
- Lior Yariv, Peter Hedman, Christian Reiser, Dor Verbin, Pratul P Srinivasan, Richard Szeliski, Jonathan T Barron, and Ben Mildenhall. Baked sdf: Meshing neural sdf for real-time view synthesis. In *ACM SIGGRAPH 2023 Conference Proceedings*, pp. 1–9, 2023.
- Weicai Ye, Xingyuan Yu, Xinyue Lan, Yuhang Ming, Jinyu Li, Hujun Bao, Zhaopeng Cui, and Guofeng Zhang. Deflow slam: Self-supervised scene motion decomposition for dynamic dense slam. *arXiv preprint arXiv:2207.08794*, 2022.
- Weicai Ye, Shuo Chen, Chong Bao, Hujun Bao, Marc Pollefeys, Zhaopeng Cui, and Guofeng Zhang. IntrinsicNeRF: Learning Intrinsic Neural Radiance Fields for Editable Novel View Synthesis. In *Proceedings of the IEEE/CVF International Conference on Computer Vision*, 2023a.
- Weicai Ye, Xinyue Lan, Shuo Chen, Yuhang Ming, Xingyuan Yu, Hujun Bao, Zhaopeng Cui, and Guofeng Zhang. Pvo: Panoptic visual odometry. In *Proceedings of the IEEE/CVF Conference on Computer Vision and Pattern Recognition (CVPR)*, pp. 9579–9589, June 2023b.
- Weicai Ye, Xinyu Chen, Ruohao Zhan, Di Huang, Xiaoshui Huang, Haoyi Zhu, Hujun Bao, Wanli Ouyang, Tong He, and Guofeng Zhang. Datap-sfm: Dynamic-aware tracking any point for robust dense structure from motion in the wild. *arxiv preprint*, 2024a.
- Weicai Ye, Hao Li, Yuanyuan Gao, Yalun Dai, Junyi Chen, Nanqing Dong, Dingwen Zhang, Hujun Bao, Wanli Ouyang, Yu Qiao, Tong He, and Guofeng Zhang. Fedsurfs: Scalable 3d surface gaussian splatting with federated learning for large scene reconstruction. *arxiv preprint*, 2024b.
- Chandan Yeshwanth, Yueh-Cheng Liu, Matthias Nießner, and Angela Dai. Scannet++: A high-fidelity dataset of 3d indoor scenes. In *Proceedings of the IEEE/CVF International Conference on Computer Vision*, pp. 12–22, 2023.
- Zehao Yu, Anpei Chen, Bozidar Antic, Songyou Peng, Apratim Bhattacharyya, Michael Niemeyer, Siyu Tang, Torsten Sattler, and Andreas Geiger. Sdfstudio: A unified framework for surface reconstruction, 2022a.
- Zehao Yu, Songyou Peng, Michael Niemeyer, Torsten Sattler, and Andreas Geiger. Monosdf: Exploring monocular geometric cues for neural implicit surface reconstruction. *Advances in neural information processing systems*, 35:25018–25032, 2022b.

Kai Zhang, Gernot Riegler, Noah Snaveley, and Vladlen Koltun. Nerf++: Analyzing and improving neural radiance fields. *arXiv preprint arXiv:2010.07492*, 2020.

Yongqiang Zhang, Zhipeng Hu, Haoqian Wu, Minda Zhao, Lincheng Li, Zhengxia Zou, and Changjie Fan. Towards unbiased volume rendering of neural implicit surfaces with geometry priors. In *Proceedings of the IEEE/CVF Conference on Computer Vision and Pattern Recognition*, pp. 4359–4368, 2023.

APPENDIX / SUPPLEMENTAL MATERIAL

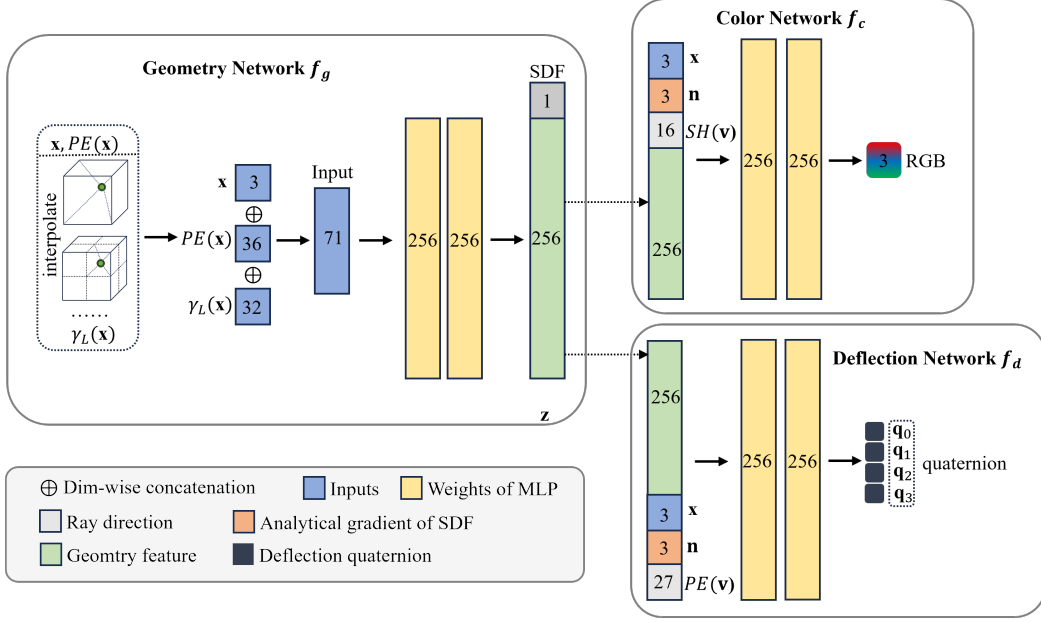


Figure 5: **Architecture of ND-SDF.** We utilize the multi-resolution hash grids γ_L as the scene representation. The geometry network f_g , color network f_c , and deflection network f_d are all constructed using simple multilayer perceptrons (MLPs).

A IMPLEMENTATION DETAILS

A.1 ARCHITECTURE

When considering the inputs to the deflection network, two scenarios are contemplated: (1) No deflection is required when the prior is entirely accurate. In this case, the quaternion axis aligns with the scene normals, thereby closely associating deflection with the scene geometry. (2) Given that the prior model is view-dependent, the quaternion for alignment with the prior must also be view-dependent. Consequently, we define:

$$\mathbf{q} = f_d(\mathbf{x}, \mathbf{v}, \mathbf{n}, \mathbf{z}), \quad (17)$$

where $\mathbf{q} = (q_0, q_1, q_2, q_3)$ represents the deflection quaternion. As detailed in Section 3.2, the quaternion can be expressed in trigonometric form as $\mathbf{q} = \cos(\theta/2) + \sin(\theta/2) (\mathbf{u}^1 i + \mathbf{u}^2 j + \mathbf{u}^3 k)$. Within the deflection network, the rotation axis is initialized along the x-axis, i.e., $\mathbf{u} = (1, 0, 0)$, and the rotation angle $\theta/2$ is set to $\pi/2$. By default, the network normalizes the output quaternions.

We observe that the structure of the deflection network mirrors that of the color network Yariv et al. (2020), denoted as $\mathbf{c} = f_c(\mathbf{x}, \mathbf{v}, \mathbf{n}, \mathbf{z})$. However, considering that the color network solely models scene-related radiance, while the deflection network encapsulates a greater extent of the prior deviation, we separate these two networks.

A.2 PROGRESSIVE WARM-UP

In the early stages of training, deflection fields would introduce negative effects such as noise. Before the rough formation of scene geometry, these deflection quaternions are random and erroneous. If unconstrained, deflecting the true normals during this initial phase can lead to reconstruction errors, such as surface protrusions.

Method	F-score
w/o warm-up	0.667
w warm-up	0.686

Table 7: **Ablation of Warm-Up Strategy.** The warm-up strategy can better facilitate the initialization of the deflection field, resulting in improved surface reconstruction quality.

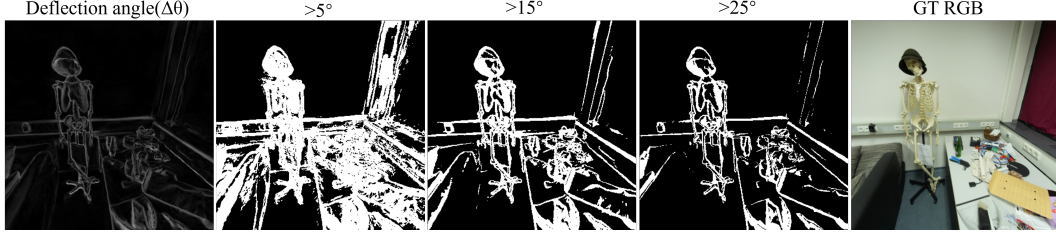


Figure 6: **Visualization of the Deflection Angle.** We visualize the angle map and the angle mask using thresholds of 5° , 15° , and 25° .

To address this issue, we propose a gradual activation strategy for deflection fields, allowing them to become effective as the surface takes shape. Specifically, we design a "quat anneal" policy to enable the deflection effect progressively. Given the surface normals synthesized by volume rendering, denoted as $\mathbf{N}(\mathbf{r})$, and the quaternion $\mathbf{Q}(\mathbf{r}) = (\mathbf{Q}_0, \mathbf{Q}_1, \mathbf{Q}_2, \mathbf{Q}_3)$, we first decompose $\mathbf{Q}(\mathbf{r})$ into its trigonometric representation:

$$\begin{aligned} \frac{\theta}{2} &= \arccos \mathbf{Q}_0 \\ \mathbf{u} &= \frac{[\mathbf{Q}_1, \mathbf{Q}_2, \mathbf{Q}_3]}{\sin \frac{\theta}{2}}. \end{aligned} \quad (18)$$

Here, \mathbf{u} represents the rotation axis corresponding to the quaternion $\mathbf{Q}(\mathbf{r})$, and θ is the rotation angle. We utilize the scene normals to warm up the deflection axis, starting with zero rotation:

$$\begin{aligned} \frac{\theta_{iter}}{2} &= prog_q \times \frac{\theta}{2} \\ \mathbf{u}_{iter} &= prog_q \times \mathbf{u} + (1 - prog_q) \times \hat{\mathbf{N}}(\mathbf{r}). \end{aligned} \quad (19)$$

Here, the parameter $prog_q$ linearly increases from 0 to 1 during the training process within the process interval $[0, anneal_quat_end]$. Once the training progress reaches $anneal_quat_end$, the warm-up phase concludes, and $prog_q$ becomes equal to 1.

The warm-up deflection quaternion is computed as:

$$\mathbf{Q}_{iter}(\mathbf{r}) = \cos \frac{\theta_{iter}}{2} + \sin \frac{\theta_{iter}}{2} \times \mathbf{u}_{iter}. \quad (20)$$

During the initial training stages, the deflection angles are close to zero, enabling us to leverage prior knowledge to learn smooth regions and approximate the scene geometry. We consider it to be adequately initialized as the warm-up phase concludes. In this process, the deflection field gradually adapts to more complex structures and deviations from the normal priors. The quantitative results with and without progressive warm-up are presented in Table 7.

A.3 MORE DETAILS

A.3.1 ADAPTIVE DEFLECTION ANGLE PRIOR LOSS

In Section 3.3, we introduce two modulation functions, namely g^d and g (Eq. 12), which adjust the weight of the deflected and original normal loss terms based on the deflection angle.

Here provide the specific form for both functions. For convenience, we employ a shifted logistic function to define them:

$$\begin{aligned} g^d(\theta) &= \frac{1}{(1 + e^{-s_0(\theta - \theta_0)})} \\ g(\theta) &= 1 - g^d(\theta) \end{aligned} \quad (21)$$

Here, the parameter s_0 controls the steepness of g^d , and θ_0 denotes the offset term. In our experiments, we set $s_0 = 12.5$, $\theta_0 = \frac{\pi}{12}$ for all scenes.

As illustrated in Figure 6, we consistently observe that a deviation angle less than 5° indicates a simple flat region, whereas a deviation angle greater than 15° largely suggests a complex structural region.

Additionally, we visualize the modulation function $g^d(\Delta\theta)$ in Figure 7. For regions with a deviation angle less than 5° , we assign weights greater than 0.9 to the original normal loss term to effectively utilize the normal priors in smooth regions.

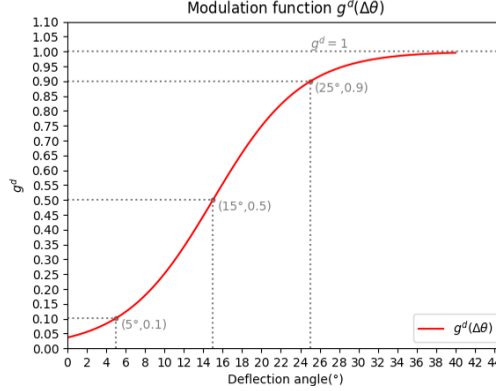


Figure 7: **Modulation Function** $g^d(\Delta\theta)$ defined in Eq. 21.

A.3.2 DEFLECTION ANGLE GUIDED OPTIMIZATION

In Section 3.4, we introduce three deflection angle guided optimization methods, including ray sampling, photometric optimization, and unbiased rendering.

To achieve ray sampling guided by the deflection angle, we dynamically maintain a deflection angle map ($\Delta\bar{\theta}$) per image during the training process. In the sampling phase, we first calculate the per-pixel sampling probability based on the deflection angle map. Then use the probability map for inverse sampling, meaning that areas with greater deflection magnitude tend to have more rays sampled.

We employ a scaled and shifted logistic function to calculate the per-pixel sampling probability:

$$p(\mathbf{r}_i) = 1 + \frac{t_1}{(1 + e^{-s_1(\Delta\bar{\theta}(\mathbf{r}_i) - \theta_1)})}, \quad (22)$$

where $\Delta\bar{\theta}$ represents the deflection angle map, and $p(\mathbf{r}_i) \in [1, t_1 + 1]$, with the steepness controlled by s_1 . We then normalize the probability map for inverse sampling using the following equation:

$$p(\mathbf{r}_i) = \frac{p(\mathbf{r}_i)}{\sum_i p(\mathbf{r}_i)}. \quad (23)$$

For the angle guided color loss, we similarly employ a scaled and shifted logistic function to re-weight the original color loss term guided by the deflection angle (Eq. 14):

$$w_{color}(\Delta\theta(\mathbf{r})) = 1 + \frac{t_2}{(1 + e^{-s_2(\Delta\theta(\mathbf{r}) - \theta_2)})}. \quad (24)$$

Regarding the angle guided unbiased rendering, we define a bias confidence using the deflection angle. Another shifted logistic function is employed to compute the bias confidence:

$$cf d(\mathbf{r}) = \frac{1}{(1 + e^{-s_3(\Delta\theta(\mathbf{r}) - \theta_3)})}. \quad (25)$$

This leads to deflection angle guided unbiasing:

$$\sigma(\mathbf{r}(t_i)) = \alpha \Psi_\beta \left(\frac{-f_g(\mathbf{r}(t_i))}{cf d(\mathbf{r}) |f'_g(\mathbf{r}(t_i))| + 1 - cf d(\mathbf{r})} \right). \quad (26)$$

In practice, we set: $(s_1 = 25, \theta_1 = \frac{\pi}{12}, t_1 = 4), (s_2 = 25, \theta_2 = \frac{\pi}{12}, t_2 = 2), (s_3 = 25, \theta_3 = \frac{\pi}{18})$.

A.3.3 NUMERICAL GRADIENT

Following Neuralangelo Li et al. (2023), we employ numerical gradients w.r.t multi-resolution hash grids to enhance reconstruction quality. The numerical gradient is computed as follows (considering only the SDF value output of f_g):

$$\nabla_x f_g(\mathbf{x}_i) = \frac{f_g(\gamma_L(\mathbf{x}_i + \epsilon_x)) - f_g(\gamma_L(\mathbf{x}_i - \epsilon_x))}{2\epsilon}. \quad (27)$$

Here, $\epsilon_x = [\epsilon, 0, 0]$ signifies the incremental step size along the x-axis. The method for calculating the numerical gradient along the y or z-axis remains the same.

We also utilize the curvature loss Li et al. (2023) to further encourage the smoothness of the reconstructed surfaces. This loss term is defined as:

$$\mathcal{L}_{\text{curv}} = \frac{1}{N} \sum_{i=1}^N |\nabla^2 f_g(\mathbf{x}_i)|. \quad (28)$$

B EXTENSIVE ABLATION STUDIES

B.1 ABLATION OF PARTIAL UNBIASED RENDERING

In Section 3.5, we introduce an unbiased function. We partially apply this technique to thin structures indicated by the learned deflection angles, without doing so may result in an inability to converge and a decrease in reconstruction quality.

We attribute this issue to the inconsistency in perspective inherent in the transform function. According to TUVR Zhang et al. (2023):

$$f'_g(\mathbf{r}(t_i)) = \nabla f_g(\mathbf{o} + t_i \mathbf{v}) \cdot \mathbf{v} = \mathbf{n}_i \cdot \mathbf{v}, \quad (29)$$

where \mathbf{v} represents the ray direction and \mathbf{n}_i denotes the normal at point \mathbf{x}_i (also $\mathbf{r}(t_i)$). We find that $\frac{\partial f_g(\mathbf{r}(t_i))}{\partial t}$ is equivalent to the cosine of ray and normal.

Consider any other ray in space, denoted as $\mathbf{r}'(t) = \mathbf{o}' + t\mathbf{v}'$. Assuming that this ray also intersects at \mathbf{x}_i and samples the same point such that $\mathbf{x}_j = \mathbf{o}' + t_j \mathbf{v}' = \mathbf{x}_i$, the volumetric density of \mathbf{x}_j under the transform function is given by:

$$\sigma(\mathbf{r}'(t_j)) = \alpha \Psi_\beta \left(\frac{-f_g(\mathbf{r}'(t_j))}{|f'_g(\mathbf{r}'(t_j))|} \right), \quad (30)$$

where $f_g(\mathbf{r}(t_i)) = f_g(\mathbf{r}(t_j))$ because $\mathbf{x}_i = \mathbf{x}_j$ and $\mathbf{n}_i = \mathbf{n}_j$, but $|f'_g(\mathbf{r}(t_i))| \neq |f'_g(\mathbf{r}(t_j))|$ because $\mathbf{n}_i \cdot \mathbf{v} \neq \mathbf{n}_j \cdot \mathbf{v}'$. The inconsistency in perspective leads to ambiguity in the volume density at the same sampling point, causing complex indoor surfaces to fail to converge. Therefore, to reduce this

Method	F-score
w/o partial	0.662
w partial	0.686

Table 8: **Ablation of Partial Unbiased Rendering.** We observed a decrease in reconstruction quality after omitting partial unbiased rendering.

Method	F-score
w/o \mathcal{L}_{depth}^d	0.664
w \mathcal{L}_{depth}^d	0.686

Table 9: **Ablation of adaptive depth prior loss.** We observed a decrease in reconstruction accuracy after omitting the adaptive depth loss.

ambiguity, we choose to apply the transform function only to fine regions indicated by the deflection angle.

The quantitative ablation results for partial unbiased rendering are presented in Table 8, where the improved F-score underscores the significance of this strategy.

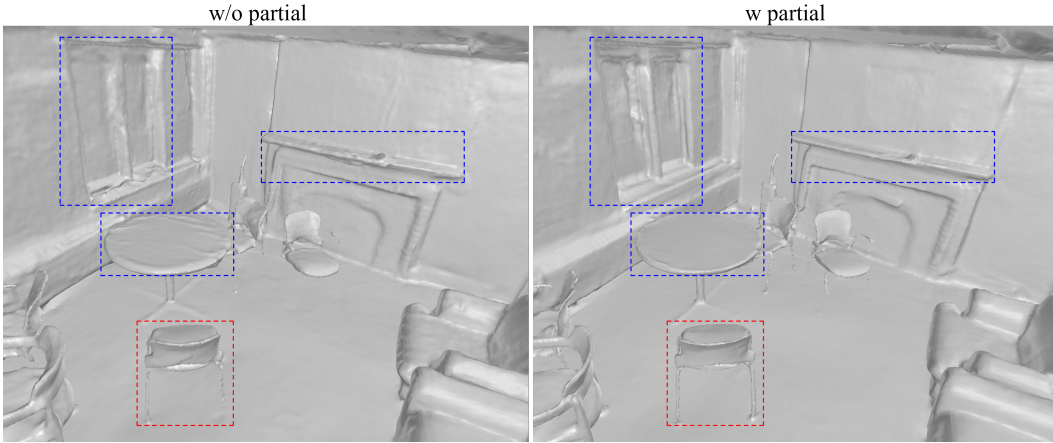


Figure 8: **Visual comparisons of partial unbiased rendering on ScanNet.**

In Figure 8, qualitative comparisons on ScanNet are presented. As indicated by the blue box, the reconstructed surfaces exhibit wrinkles and irregularities without the application of the proposed partial unbiased rendering strategy and fail to capture the fine structural details of the chair legs highlighted in the red box. After applying the strategy, the overall surface becomes precise and smooth. These visual results demonstrate the superiority of the proposed partial unbiased rendering method.

B.2 ABLATION OF ADAPTIVE MONOCULAR DEPTH LOSS

Notably, we use the same method to adjust depth supervision (Eq. 13) based on deflection angle. This simplified treatment rests on a strong foundation for two reasons. First, both the depth and normal cues originate from the same pretrained model Eftekhar et al. (2021) and share a common inductive bias. Second, monocular depth lacks scale and cannot provide accurate supervision. In implicit surface reconstruction with priors, depth cues are primarily utilized to facilitate convergence and accelerate surface formation. Automatically and continuously masking high-frequency areas based on the deflection angle has no adverse impact on the recovery of details.

We present the quantitative ablation results in Table 9. The improved performance underscores the importance of utilizing the adaptive deflection angle depth prior loss.

Method	036bce3393						0e75f3c4d9					
	Acc↓	Comp↓	Pre↑	Recall↑	Chamfer↓	F-score↑	Acc↓	Comp↓	Pre↑	Recall↑	Chamfer↓	F-score↑
VolSDF	0.053	0.098	0.475	0.372	0.0755	0.417	0.053	0.078	0.395	0.363	0.065	0.378
Baked-Angelo	0.168	0.023	0.52	0.78	0.0955	0.624	0.121	0.053	0.525	0.719	0.087	0.607
MonoSDF	0.037	0.037	0.606	0.656	0.037	0.630	0.064	0.027	0.574	0.705	0.046	0.633
ND-SDF	0.037	0.031	0.648	0.728	0.034	0.686	0.054	0.018	0.662	0.864	0.036	0.750

Method	108ec0b806						7f4d173c9c					
	Acc↓	Comp↓	Pre↑	Recall↑	Chamfer↓	F-score↑	Acc↓	Comp↓	Pre↑	Recall↑	Chamfer↓	F-score↑
VolSDF	0.049	0.097	0.475	0.372	0.073	0.417	0.097	0.075	0.457	0.436	0.086	0.446
Baked-Angelo	0.092	0.050	0.498	0.624	0.071	0.554	0.420	0.024	0.457	0.799	0.222	0.582
MonoSDF	0.041	0.045	0.575	0.576	0.043	0.576	0.138	0.022	0.708	0.813	0.080	0.757
ND-SDF	0.047	0.040	0.591	0.646	0.044	0.617	0.112	0.015	0.721	0.888	0.064	0.796

Method	ab11145646						e050c15a8d					
	Acc↓	Comp↓	Pre↑	Recall↑	Chamfer↓	F-score↑	Acc↓	Comp↓	Pre↑	Recall↑	Chamfer↓	F-score↑
VolSDF	0.089	0.164	0.321	0.226	0.126	0.265	0.077	0.101	0.307	0.262	0.089	0.283
Baked-Angelo	0.076	0.038	0.575	0.701	0.057	0.632	0.034	0.043	0.685	0.687	0.038	0.686
MonoSDF	0.036	0.035	0.695	0.700	0.036	0.697	0.027	0.024	0.747	0.770	0.026	0.758
ND-SDF	0.054	0.024	0.657	0.786	0.039	0.716	0.036	0.020	0.723	0.798	0.028	0.759

Table 10: **Quantitative results of the 6 selected scenes from ScanNet++.** Our method achieves state-of-the-art performance.

C MORE RESULTS

C.1 REPLICAS

We present additional visualization results on Replica in Figure 9.

C.2 SCANNET++

We present detailed quantitative results of the selected six scenes from ScanNet++ in Table 10 and provide more visualization results in Figure 10. Compared to the baselines, our method yields significantly improved reconstructions both visually and quantitatively. Notably, our method contributes substantially to capturing thin and fine-grained structures.

C.3 TANKS AND TEMPLES

We present additional qualitative comparisons with previous state-of-the-art baselines, including MonoSDF Yu et al. (2022b) and NeurIS Yu et al. (2022b), as depicted in Figure 11. Notably, ND-SDF achieves accurate dense surfaces replete with extensive details.

As illustrated in Figure 12 and Figure 13, we further extracted the reconstructed mesh at a resolution of 2048. The mesh, with this resolution, demonstrates that our method significantly enhances the generation of small and complex structures, even in challenging large-scale indoor scenes. The hash grid for all experiments remains at the default settings, with resolutions spanning from 2^5 to 2^{11} across 16 levels, and the size of hashmap staying at 2^{19} .

C.4 MORE INFORMATION ABOUT DATASET

The qualitative results on ScanNet in the main content demonstrate that our method can capture fine details, such as the chair legs, which are even missed by the ground truth (GT). This highlights a known issue regarding the reliability of ScanNet GT meshes. The ScanNet dataset, constructed in 2017, is based on RGB-D data captured by an iPad with an additional structure sensor. The images have relatively low resolution and suffer from motion blur and lighting variations. In addition, due to the limitations of the bundle-fusion algorithm, the GT surfaces lack fine structures, which can lead to a decrease in evaluation performance in these areas. This also explains why we tend to conduct quantitative ablation studies on ScanNet++, which provides more reliable evaluation results.

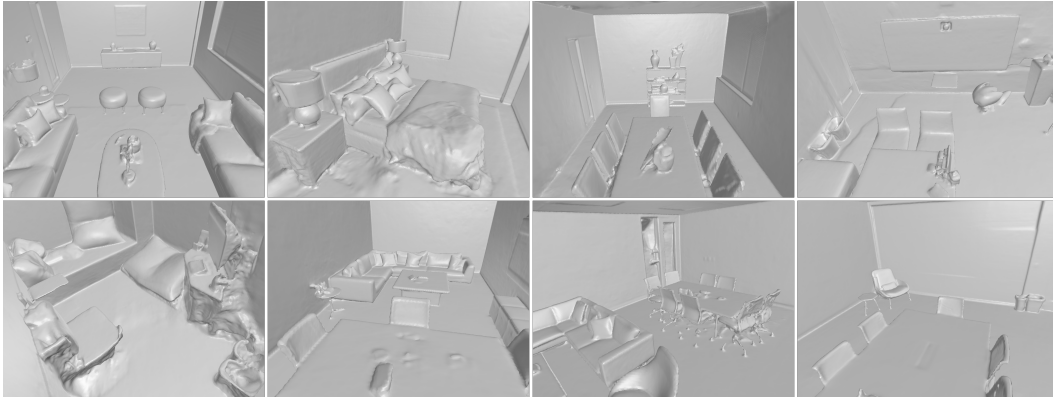


Figure 9: **Visualization results on Replica dataset.**

D SOCIETAL IMPACT

Our method contributes to high-fidelity indoor surface reconstruction. On the positive side, precise indoor surface reconstruction can revolutionize fields such as architecture, virtual reality, and robotics. It enables architects to visualize and optimize designs, enhances immersive experiences in virtual environments, and aids in navigation for autonomous robots. However, there are also challenges. Misuse of this technology could invade privacy, as detailed indoor reconstructions might reveal sensitive information. Striking a balance between innovation and responsible deployment will be crucial for maximizing the positive impact while minimizing potential harm.

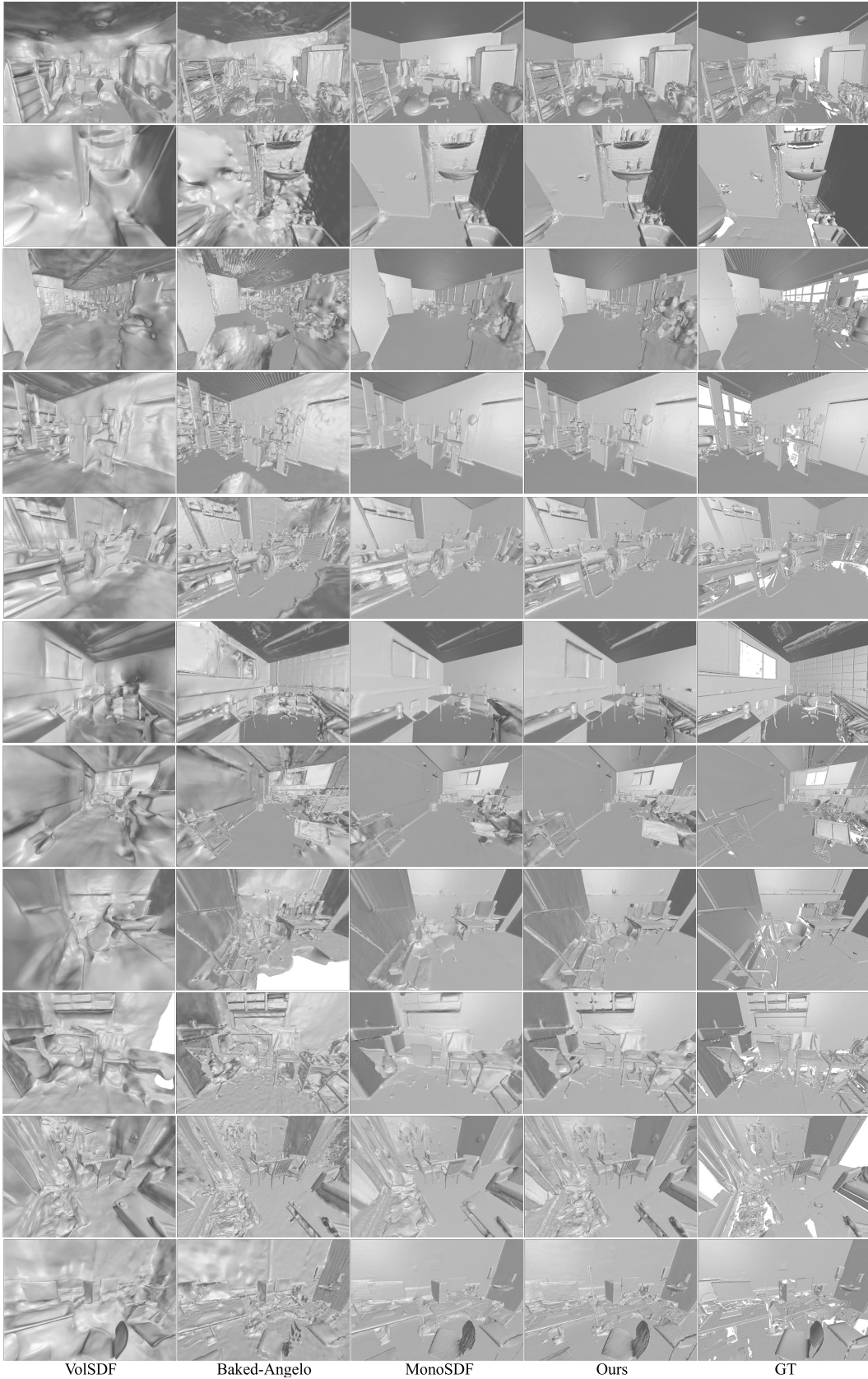


Figure 10: **Qualitative Comparison on ScanNet++.** We compare ND-SDF with several baseline methods, including VolSDF, Baked-Angelo, and MonoSDF. Notably, only MonoSDF leveraged monocular priors. Our method facilitates both smoothness and details, while MonoSDF loses substantial fine structures, and Baked-Angelo cannot handle textureless smooth regions such as floors.



Figure 11: **Qualitative Comparison on Tanks & Temples.** We compare ND-SDF with previous state-of-the-art indoor implicit reconstruction methods.



Figure 12: **Qualitative Comparison of Different extraction resolutions on Tanks & Temples.** We additionally extract the recovered mesh from the implicit SDF at a resolution of 2048.

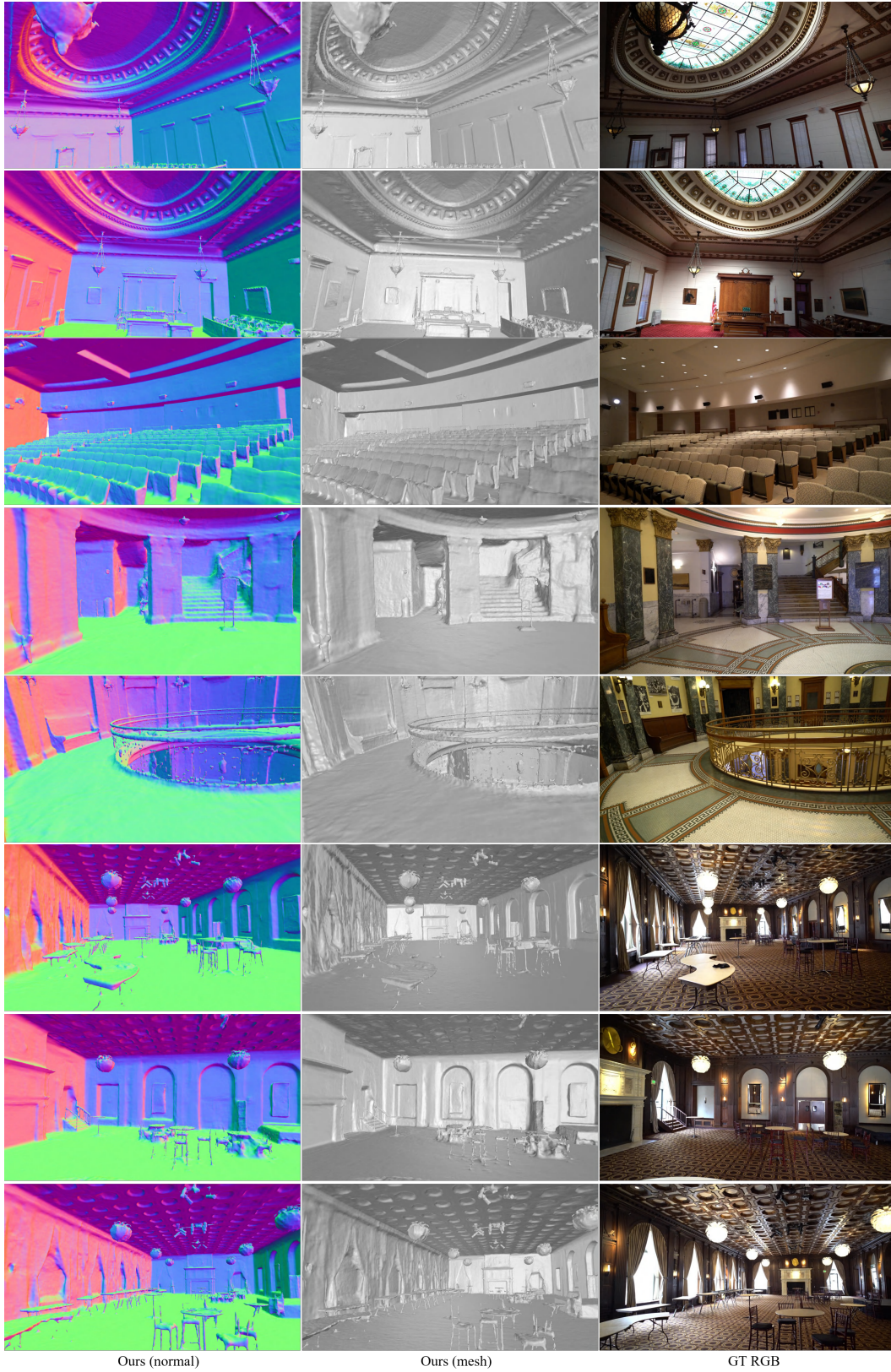


Figure 13: **Qualitative Results of the extracted mesh at a resolution of 2048 on Tanks & Temples.**